

Isogeometric Multi-Resolution Full Waveform Inversion based on the Finite Cell Method

Tim Burchner^{*1}, Philipp Kopp¹, Stefan Kollmannsberger¹ and Ernst Rank^{1, 2}

¹Chair of Computational Modeling and Simulation, Technische Universität München

²Institute for Advanced Study, Technische Universität München

Abstract

Full waveform inversion (FWI) is an iterative identification process that serves to minimize the misfit of model-based simulated and experimentally measured wave field data, with the goal of identifying a field of parameters for a given physical object. For many years, FWI has been used very successfully in seismic imaging to deduce velocity models of the earth or of local geophysical exploration areas. FWI has also been successfully applied in various other fields, including non-destructive testing (NDT) and biomedical imaging. The inverse optimization process of FWI is based on forward and backward solutions of the (elastic or acoustic) wave equation, as well as on efficient computation of an adequate optimization direction. Many approaches use (low order) finite element or finite difference methods, often with a field of parameter values with a resolution corresponding to elements or nodes of the discretized wave field. In a previous paper [1], we explored opportunities of using the finite cell method (FCM) as the wave field solver, which has the advantage that highly complex geometric models can be incorporated easily. Furthermore, we demonstrated that the identification of the model's density outperforms that of the velocity – particularly in cases where unknown voids characterized by homogeneous Neumann boundary conditions need to be detected. The paper at hand extends this previous study in the following aspects: The isogeometric finite cell analysis (IGA-FCM) – a combination of isogeometric analysis (IGA) and FCM – is applied for the wave field solver, with the advantage that the polynomial degree and subsequently also the sampling frequency of the wave field can be increased quite easily. Since the inversion efficiency strongly depends on the accuracy of the forward and backward wave field solution and of the gradient of the functional, consistent and lumped mass matrix discretization are compared. The resolution of the grid describing the unknown material density – thus allowing to identify voids in a physical object – is then decoupled from the knot span grid. Finally, we propose an adaptive multi-resolution algorithm that refines the material grid only locally using an image processing-based refinement indicator. The developed inversion framework allows fast and memory-efficient wave simulation and object identification. While we study the general behavior of the proposed approach on 2D benchmark problems, a final 3D problem shows that it can also be used to identify void regions in geometrically complex spatial structures.

Keywords: full waveform inversion, isogeometric analysis, finite cell method, multi-resolution, scalar wave equation

1 Introduction

Tom Hughes has initiated and driven countless innovations in computational science and engineering. Among the most important is undoubtedly the invention of isogeometric analysis. Originally motivated by the goal of uniting the separate worlds of geometric modeling and finite element analysis,

^{*}tim.buerchner@tum.de, Corresponding author

the great value of this method is also demonstrated by the fact that new areas of application continue to emerge that were not part of the original objective. The present contribution is exactly of this kind. We show how unknown geometric features of a structure can be effectively identified, and how an inverse analysis benefits from superior inherent properties of IGA, such as the ability to obtain highly accurate results with a small number of degrees of freedom.

Happy Birthday, Tom.

With its origins in the 1980s [2, 3], full waveform inversion (FWI) has become a well-established method in the field of seismic tomography. Waves traveling through the interior of a medium are measured and compared to model-based simulated wave signals. Information about internal material properties is extracted in a nonlinear optimization problem. The adjoint method using forward and backward simulations of the wave field allows for an efficient use of gradient-based optimization [4]. A comprehensive introduction to FWI can be found in [5], reviews in [6, 7].

While FWI has been used very successfully in geophysics for a long time, its application to biomedical applications [8–10] and non-destructive testing (NDT) [11–13] has gained traction in recent years. In these problems, the goal often is to identify interior voids or fractures characterized by homogeneous Neumann boundary conditions. Such defects are challenging to detect using classical velocity-based FWI. In previous work [1], we showed that density inversion allows to efficiently identify and reconstruct these defects in possibly damaged samples. A thorough analysis of the distinct behaviors of density and velocity inversion based on a boundary layer description is provided in [14]. To ensure the success of FWI, it is crucial to efficiently and precisely solve the forward and backward wave problems – and to construct an accurate and sufficiently resolved material description. However, many numerical schemes couple the wave field discretization and material representation, which does not allow to freely adapt them independently of each other. It is common to use a finite difference grid or a finite element mesh for the wave field to describe a material as constant per element or interpolated by a nodal-based Ansatz using shape functions defined on sub-blocks of the elements (e.g. [15, 16]). Nevertheless, this description is often closely tied to the spectral element method (SEM) and not more than $p + 1$ sub-blocks can be captured by the integration per element. The focus of the present contribution is to investigate the interactions between the wave field discretization and a completely independent material representation. Consequently, two key questions arise: Which high-order schemes are suitable to solve the forward and backward wave equation, and how can an independent yet efficient description of the material field be realized?

In general, high-order finite element methods outperform low-order approaches in approximating smooth wave solutions. Thanks to its diagonal mass matrix, the SEM is very popular in combination with explicit time stepping [17]. However, the diagonal structure of the mass matrix is a consequence of employing Lagrange basis functions in combination with Gauss Legendre Lobatto (GLL) quadrature [18, 19]. If a material discretization is chosen that requires a different integration scheme, the diagonality and hence the central advantage of SEM in explicit time integration is lost. As an alternative to SEM, we use isogeometric analysis (IGA) [20] and an independent voxel-based material representation in the paper at hand to study the interaction between the wave field discretization and the resolution of the material field. The higher spline continuity across knot span boundaries allows to accurately solve wave problems with a significant lower number of degrees of freedom [21]. To easily incorporate complex geometric features of a structure, the finite cell method (FCM) [22] is used. The isogeometric finite cell analysis (IGA-FCM) – a combination of trimmed IGA and FCM – has been previously studied in [23] and [24] in the context of linear elasticity, and has later been extended to dynamic problems [25, 26]. Similar approaches and in particular detailed mathematical analyses of IGA and immersed boundary methods are provided in the vast literature on CutFEM, e.g. [27, 28].

The paper at hand combines an IGA-FCM approximation of the wave field with a voxelized representation of the material parameter. The subsequent key aspects of this multi-resolution FWI approach are addressed:

- First, the forward simulation of the scalar wave equation using the consistent and row-sum lumped version of IGA-FCM is investigated – with the goal to assess their suitability for an IGA-based FWI.

- Second, the paper examines the interaction between the resolutions of the wave field and the material field for the inverse problem in terms of accuracy and computational cost.
- Third, an adaptive locally refined material grid is introduced as part of the inversion process. The efficiency of this approach is demonstrated with 2D and 3D examples.

This paper is the second contribution in a sequence applying immersed boundary methods to full waveform inversion. To ensure self-consistency, the basics introduced in the first paper [1] are briefly summarized. It is structured as follows: In Section 2, we introduce the scalar wave equation, its spatial and temporal discretization, and the corresponding optimization problem. Section 3 derives guidelines for the discretization of the wave field with IGA-FCM and its row-sum lumped variant for the forward wave problem. Section 4 deals with the inverse problem, where the multi-resolution approach is evaluated on a 2D example. We then introduce an adaptive local refinement in the material field and apply the developed methodology to 2D and 3D examples. Finally, we conclude the paper in Section 5.

2 Full waveform inversion by isogeometric finite cell analysis

2.1 FCM for the scalar wave equation

We briefly summarize the nomenclature used in [1], assuming an isotropic heterogeneous medium with density $\rho(\mathbf{x})$ and wave speed $c(\mathbf{x})$. Introducing the wave field $u(\mathbf{x}, t)$, its acceleration $\ddot{u}(\mathbf{x}, t)$ and the external force term $f(\mathbf{x}, t)$, the scalar wave equation is defined on a computational domain Ω for the time $\mathcal{T} = [0, T_{\max}]$

$$\rho(\mathbf{x})\ddot{u}(\mathbf{x}, t) - \nabla \cdot (\rho(\mathbf{x})c^2(\mathbf{x})\nabla u(\mathbf{x}, t)) = f(\mathbf{x}, t), \quad \mathbf{x} \in \Omega, t \in \mathcal{T}. \quad (1)$$

The initial conditions are $u(\mathbf{x}, 0) = \dot{u}(\mathbf{x}, 0) = 0$ for $\mathbf{x} \in \Omega$, the boundary conditions $u(\mathbf{x}, t) = 0, \mathbf{x} \in \partial\Omega_D$ and $\mathbf{n} \cdot \nabla u(\mathbf{x}, t) = 0, \mathbf{x} \in \partial\Omega_N$ with $\partial\Omega = \partial\Omega_D \cup \partial\Omega_N$. We assume that a density ρ_0 and wave speed c_0 of the background material are given.

All known geometric features of a structure are incorporated in the initial domain Ω , which may itself already have complex geometric shape. Applying the basic concept of the finite cell method, Ω is embedded in a larger, yet simply shaped domain Ω_e . The original domain Ω is recovered through an indicator function $\alpha(\mathbf{x})$, which assumes a small value ϵ (typically 10^{-5} to 10^{-8}) representing a small density in the fictitious part of Ω_e . While $\alpha(\mathbf{x})$ is known a priori, unknown defects in the structure are iteratively identified by reconstructing a second, unknown scaling function $\gamma(\mathbf{x})$, see Figure 1. Since α and γ only scale the density, the scalar wave equation takes the following form on the extended domain Ω_e

$$\alpha(\mathbf{x})\gamma(\mathbf{x})\rho_0\ddot{u}(\mathbf{x}, t) - \nabla \cdot (\alpha(\mathbf{x})\gamma(\mathbf{x})\rho_0c_0^2\nabla u(\mathbf{x}, t)) = f(\mathbf{x}, t), \quad \mathbf{x} \in \Omega_e, t \in \mathcal{T}. \quad (2)$$

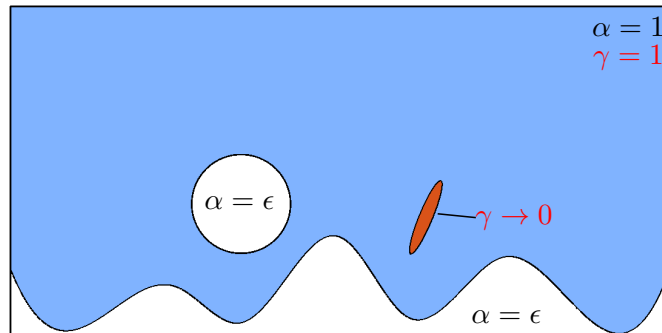


Figure 1: A priori known geometry incorporated by the indicator function α with an unknown void reconstructed by the scaling function γ (from [1])

Note that this approach is independent of the basis chosen to discretize the spatial solution field. The spectral cell method (SCM) [29, 30] uses Lagrange polynomials to approximate the wave field for both scalar and elastic wave equations. Isogeometric finite cell analysis (IGA-FCM) published in [23, 24] can be combined with mass lumping to be used in explicit dynamics [31, 26, 32]. Other immersed boundary methods (IBM) closely related to FCM are CutFEM [27, 33], IBRA [34], aggregated FEM [35], cgFEM [36], and the shifted boundary method [37, 38]. Common to all these approaches is the idea to circumvent the task of boundary-conforming mesh generation by generating a non-boundary conforming computational grid and recovering the boundary at the level of the integration of the underlying bilinear forms. Obviously, this does not come at zero cost. In FCM, the integrands of the element mass and stiffness matrices are discontinuous for cells cut by boundaries of the physical domain. Several suitable integration approaches have been proposed to overcome this difficulty, including space-trees [39, 40], moment-fitting [41], local integration meshes [42], or smart octrees [43]. In [44], it is shown that FCM can be combined with a voxelized representation of the material parameter α . The integration is performed on a finer voxel grid using pre-integration to mitigate the computational burden of computing the system matrices [45].

2.2 Spatial discretization of the wave field and material

For the approximation of the wave field $u(\mathbf{x}, t)$, we use bivariate and trivariate B-spline discretizations in 2D and 3D [20, 46]. By defining a polynomial degree p and a set of parametric coordinates, called the knot vector $\Xi = [\xi_1, \xi_2, \dots, \xi_{n+p+1}]$, the B-spline basis functions can be constructed – where ξ_i is the i th knot and n the number of basis functions. Using the Cox-de Boor recursion formula [47, 48], the B-splines are

$$N_{i,0}(\xi) = \begin{cases} 1, & \xi_i \leq \xi < \xi_{i+1} \\ 0, & \text{otherwise} \end{cases}, \quad \text{if } p = 0 \quad (3)$$

$$N_{i,p}(\xi) = \frac{\xi - \xi_i}{\xi_{i+p} - \xi_i} N_{i,p-1}(\xi) + \frac{\xi_{i+p+1} - \xi}{\xi_{i+p+1} - \xi_{i+1}} N_{i+1,p-1}(\xi) \quad \text{else.} \quad (4)$$

The continuity C^{p-k} of B-splines across the knot boundaries is defined by the knot multiplicity k . Henceforth, unless otherwise indicated we use open knot vectors with $k = 1$ for all inner knots and $k = p + 1$ for the end knot. With the set of all n^{dof} bi- or trivariate basis functions \mathbf{N} , the spatially discretized wave solution is

$$u(\mathbf{x}, t) \approx \tilde{u}(\mathbf{x}, t) = \sum_{i=1}^{n^{\text{dof}}} N_i(\mathbf{x}) \hat{u}_i(t) = \mathbf{N}(\mathbf{x}) \hat{\mathbf{u}}(t), \quad (5)$$

where \hat{u}_i are the coefficients of the corresponding basis functions. Thanks to the non-negative partition of unity property of B-splines [49], row-sum lumping is readily applicable and has been revived for boundary-conforming [50] and immersed IGA [31, 26]. Unfortunately, row-summing leads to a breakdown of p -convergence. As shown in [50], the convergence of the first generalized eigenvalue is only of quadratic order for quadratic and cubic B-splines in 1D problems. Nevertheless, row-summing leads to a critical time step that becomes independent from the cut ratio of the knot spans if the physical domain is immersed [25, 26, 32] and, therefore – at least at first sight – seems to be an attractive option for explicit dynamics.

For the discretization of the material parameters, we utilize piecewise constant functions $N_{m,i}$ defined on a voxel grid (see Figure 2).

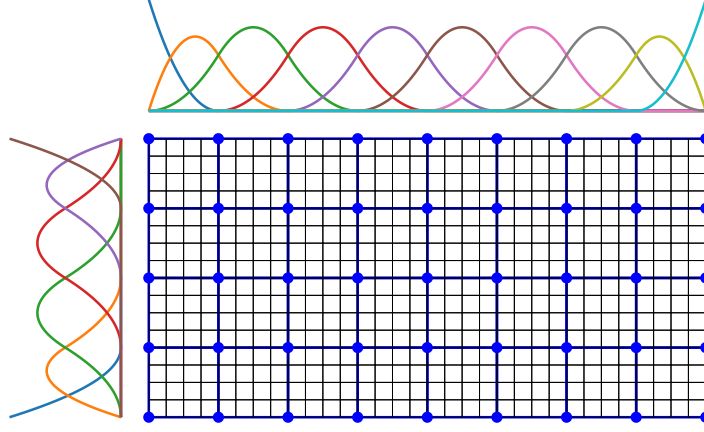


Figure 2: Wave field mesh (thick blue lines and nodes) and material mesh (thin black lines)

While this material grid can, in principle, be fully independent of the knot span grid for the spatial wave discretization, it is computationally advantageous to define it as a refinement with n^v voxels per knot span in each spatial direction. With n^m voxels discretizing the complete extended domain Ω_e , the material discretization is

$$\gamma(\mathbf{x}) \approx \tilde{\gamma}(\mathbf{x}) = \sum_{i=1}^{n^m} N_{m,i}(\mathbf{x}) \hat{\gamma}_i = \mathbf{N}_m(\mathbf{x}) \hat{\gamma}, \quad (6)$$

where $\hat{\gamma}_i$ denotes the value of the voxel. Since the material might be discontinuous within one knot span, the integration of the mass and stiffness matrices is performed by means of a composed integration at the voxel level, as e.g. [44].

2.3 Time integration

Derived by the Bubnov-Galerkin approach, we introduce the mass matrix \mathbf{M} , the stiffness matrix \mathbf{K} and the external force vector \mathbf{F} . The space-discrete form of the scalar wave equation is given by

$$\mathbf{M}\ddot{\mathbf{u}}(t) + \mathbf{K}\mathbf{u}(t) = \hat{\mathbf{f}}(t). \quad (7)$$

Applying second-order central differences (CDM), the next time step $t_{i+1} = t_i + \Delta t$ is calculated from the previous two time steps t_i and $t_{i-1} = t_i - \Delta t$:

$$\hat{\mathbf{u}}(t_{i+1}) = 2\hat{\mathbf{u}}(t_i) - \hat{\mathbf{u}}(t_{i-1}) + \Delta t^2 \mathbf{M}^{-1} [\hat{\mathbf{f}}(t_i) - \mathbf{K}\hat{\mathbf{u}}(t_i)]. \quad (8)$$

CDM is an explicit, conditionally stable time integration method. The number of time steps is denoted as n^t . The critical time step is given by

$$\Delta t_c = \frac{2}{\sqrt{\lambda_{\max}(\mathbf{K}, \mathbf{M})}}, \quad (9)$$

where $\lambda_{\max}(\mathbf{K}, \mathbf{M})$ is the largest eigenvalue of the generalized eigenproblem [49]. For details see e.g. [51].

2.4 Full waveform inversion

The goal of FWI is to find a set of unknown material coefficients $\hat{\gamma}$ to minimize the nonlinear optimization problem

$$\hat{\gamma}^* = \arg \min_{\hat{\gamma}} \chi(\hat{\gamma}). \quad (10)$$

The cost function is defined by the squared residual between simulation and experiments, summed up over n^r receiver positions in n^s experiments

$$\chi(\hat{\gamma}) = \frac{1}{2} \sum_{s=1}^{n^s} \sum_{r=1}^{n^r} \int_T \int_{\Omega} \left[\left(u^s(\hat{\gamma}; \mathbf{x}, t) - u^{0,s}(\mathbf{x}, t) \right)^2 \delta(\mathbf{x} - \mathbf{x}^r) \right] d\Omega dt, \quad (11)$$

where $u^s(\hat{\gamma}; \mathbf{x}, t)$ is the solution of a wave simulation with the current material $\hat{\gamma}$ and $u^{0,s}(\mathbf{x}^r, t)$ is the corresponding experimental measurement at the receiver position \mathbf{x}^r . A typical experimental setup can be found in [1], and the computation of the gradient applying the adjoint method is derived according to [52, 53]. In the following, we revise the derived formulas from [1]. The sensitivity kernel with respect to the scaling function γ for a given set $\hat{\gamma}$ is

$$K_{\gamma}(\mathbf{x}) = \sum_{s=1}^{n^s} \int_T \left[-\alpha(\mathbf{x}) \rho_0 \dot{u}^{s,\dagger}(\hat{\gamma}; \mathbf{x}, t) \dot{u}^s(\hat{\gamma}; \mathbf{x}, t) + \alpha(\mathbf{x}) \rho_0 c_0^2 \nabla u^{s,\dagger}(\hat{\gamma}; \mathbf{x}, t) \cdot \nabla u^s(\hat{\gamma}; \mathbf{x}, t) \right] dt, \quad (12)$$

where $u^{s,\dagger}$ is the adjoint solution of experiment s . The gradient with respect to the voxel coefficients γ_i is approximated by evaluating the sensitivity kernel at the voxel mid positions $\mathbf{x}_{\hat{\gamma},i}$

$$\frac{d\chi}{d\gamma_i} \approx \int_{\Omega} K_{\gamma} \delta(\mathbf{x}_{\hat{\gamma},i} - \mathbf{x}) d\Omega = K_{\gamma}(\mathbf{x}_{\hat{\gamma},i}) \quad (13)$$

or in discretized form

$$\frac{d\chi}{d\gamma_i} \approx \sum_{s=1}^{n^s} \int_{\Omega} \int_T \left[-\rho_0 (\dot{\mathbf{u}}^{s,\dagger})^T \mathbf{N}^T \mathbf{N} \dot{\mathbf{u}}^s + \rho_0 c_0^2 (\dot{\mathbf{u}}^{s,\dagger})^T \mathbf{B}^T \mathbf{B} \dot{\mathbf{u}}^s \right] dt \delta(\mathbf{x}_{\hat{\gamma},i} - \mathbf{x}) d\Omega \quad (14)$$

The unknown material field γ is optimized only within the physical domain. Therefore, it is assumed that the indicator function α at the considered positions $\mathbf{x}_{\hat{\gamma},i}$ is equal to 1 and, consequently that it vanishes in the above equation. In gradient-based optimization, the material is iteratively improved with an update step $\Delta\hat{\gamma}$. The superscript k denotes the current iteration

$$\hat{\gamma}^{(k+1)} = \hat{\gamma}^{(k)} + \Delta\hat{\gamma}^{(k)} \quad (15)$$

Quasi-Newton type methods take into account the current gradient $\nabla_{\hat{\gamma}} \chi(\hat{\gamma}^{(k)})$ and an approximate of the inverse Hessian $\mathbf{H}_a^{-1}(\hat{\gamma}^{(k)})$ in the model update

$$\Delta\hat{\gamma}^{(k)} = -\mathbf{H}_a^{-1}(\hat{\gamma}^{(k)}) \nabla_{\hat{\gamma}} \chi(\hat{\gamma}^{(k)}). \quad (16)$$

For an introduction to gradient-based optimization, we refer to [54]. In the paper at hand, the matrix-free and bounded L-BFGS-B of the Python library SciPy [55] is applied.

The computational cost and memory requirement of the gradient computation can be readily estimated. Considering (14), the sensitivity kernel must be computed for all n^m voxel mid points. Assuming that the forward and adjoint solutions $\dot{\mathbf{u}}^s$ and $\dot{\mathbf{u}}^{s,\dagger}$ have been computed and are temporarily stored for all time steps n^t , the integrand is evaluated and summed up for all time steps. Since the evaluation is done locally for every voxel, only the $n^{\text{dof,local}}$ coefficients associated with the basis functions being non-zero in the corresponding knot span need to be considered. For the chosen wave field discretization (see Figure 2), $(p+1)^d$ non-zero basis functions exist at every position in space, where d is the spatial dimension and p is the chosen polynomial order. To summarize, the computational effort is

$$\mathcal{O}(n^s \times n^t \times n^{\text{dof,local}} \times n^m) = \mathcal{O}(n^s \times n^t \times p^d \times n^m). \quad (17)$$

Memory requirement is

$$\mathcal{O}(n^t \times n^{\text{dof}}). \quad (18)$$

For a chosen polynomial degree p , the computational effort depends only on the *total* number of voxels n^m , and on the relation between the size of the knot span and the voxel size. Since the computation of the gradient consumes a large fraction of the overall effort, insight into an optimized relationship between the resolutions of the wave field and the material grid is desirable (see Section 4).

3 Solving the wave equation by IGA-FCM

In this section, we first investigate whether IGA-FCM is generally suitable as a wave equation solver in the framework of full waveform inversion. The following observations are important:

1. A wave equation solver should allow a high convergence rate which can even be selected depending on the expected smoothness of the wave field. It is well known [20, 21] that increasing the polynomial degree of the Ansatz functions outperforms a refinement of the mesh (h-extension) by far. Therefore, IGA (like other high-order solvers) is well qualified in the context of consideration. This applies in particular in combination with immersed methods such as the FCM, as restrictions on the geometric shape of the domain Ω are minimal.
2. A solver should provide high accuracy per degree of freedom. k -extension of IGA (see [20]) combines the increase of the polynomial degree and the increase of the smoothness of the Ansatz in such a way that one degree of freedom per spatial direction is enough to gain one additional order of convergence. The computational effort associated with this additional degree of freedom may be significant due to a loss of sparsity and an increase of fill-in throughout the system matrices. Yet, the additional computational cost is offset by a drastic reduction in memory requirements. This is important because, in the adjoint gradient computation, the coefficients of the solution vectors of all time steps of the forward simulation must be stored temporarily.
3. The goal of FWI is to identify geometric features that may be small compared to the mesh size of the wave field discretization. This can be achieved (as will be shown in the following section) by using a material grid that is refined compared to the mesh of the wave field.

Let us now take a look at the IGA-FCM solution of the scalar wave problem using consistent and lumped mass matrices. We consider a two-dimensional domain of $l_x = 10$ and $l_y = 5$ with a circular hole of radius $r = 0.5$ at position $x_c = 6$ and $y_c = 2.85$, shown in Figure 3. The density and wave speed of the background material are set to $\rho_0 = 1$ and $c_0 = 1$. A 2-cycle sine burst

$$g(t) = \begin{cases} \sin(2\pi ft) \sin\left(\frac{\pi f}{2}\right) & , t \leq \frac{2}{f} \\ 0 & , \text{else} \end{cases} \quad (19)$$

with a central frequency $f = 0.5$ and a spatial Gaussian distribution

$$f(x, y) = e^{-\left(\frac{(x-x_s)^2}{2\sigma_x^2} + \frac{(y-y_s)^2}{2\sigma_y^2}\right)} \quad (20)$$

is excited at position $x_s = 2$ and $y_s = 2.5$ with $\sigma_x = \sigma_y = 0.25$, leading to a dominant wavelength $\lambda_{\text{dom}} = 2$. The wave propagation is computed for $T_{\text{max}} = 10$.

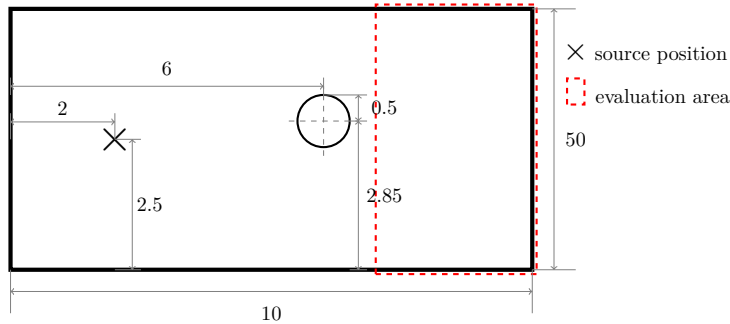


Figure 3: 2D domain with a hole

To compare the accuracy of consistent and lumped IGA-FCM for different polynomial orders, the wave solution at T_{max} is evaluated in the marked area $[7, 10] \times [0, 5]$ on the right side of the hole.

For this purpose, this area is sampled with $N_e = 601 \times 1001$ equidistant evaluation points in x - and y -direction. These evaluation points correspond to an arbitrary number of receiver positions in the FWI. The normalized error with respect to an overkill reference solution u_{ref}

$$\epsilon = \frac{\sqrt{\sum_{e=0}^{N_e} (u(\mathbf{x}_e, T_{\max}) - u_{\text{ref}}(\mathbf{x}_e, T_{\max}))^2}}{\sqrt{\sum_{e=0}^{N_e} (u_{\text{ref}}(\mathbf{x}_e, T_{\max}))^2}}. \quad (21)$$

can be interpreted as an error proportional to the \mathcal{L}_2 error calculated using the Riemann sum for integration. The reference solution is obtained with quintic C^0 continuous integrated Legendre polynomials defined on a mesh of mesh size $h = \frac{1}{16}$, resulting in 160 elements in x -direction and 80 elements in y -direction. The FCM indicator function defining the physical part of the computational domain is set to $\alpha = 10^{-8}$ inside the hole. For the consistent and lumped version of IGA-FCM, the solution is computed for linear, quadratic, cubic and quartic C^{p-1} B-splines. The mesh size is varied using $h = \frac{1}{2}, \frac{1}{4}, \frac{1}{8}, \frac{1}{16}, \frac{1}{32}$. In order to reduce spatial and temporal integration errors to a minimum, all simulations are carried out with $n^t = 100\,000$ time steps – and the integration of the mass and stiffness matrices and the force vector is performed by a quadtree-quadrature applying a depth of $d = 10$. Figure 4 shows the results for the consistent version of IGA-FCM, referred to as ‘c-IGA-FCM’, and for the lumped version of IGA-FCM, denoted as ‘l-IGA-FCM’. Reference lines proportional to h^2 , h^3 , h^4 , and h^5 are depicted.

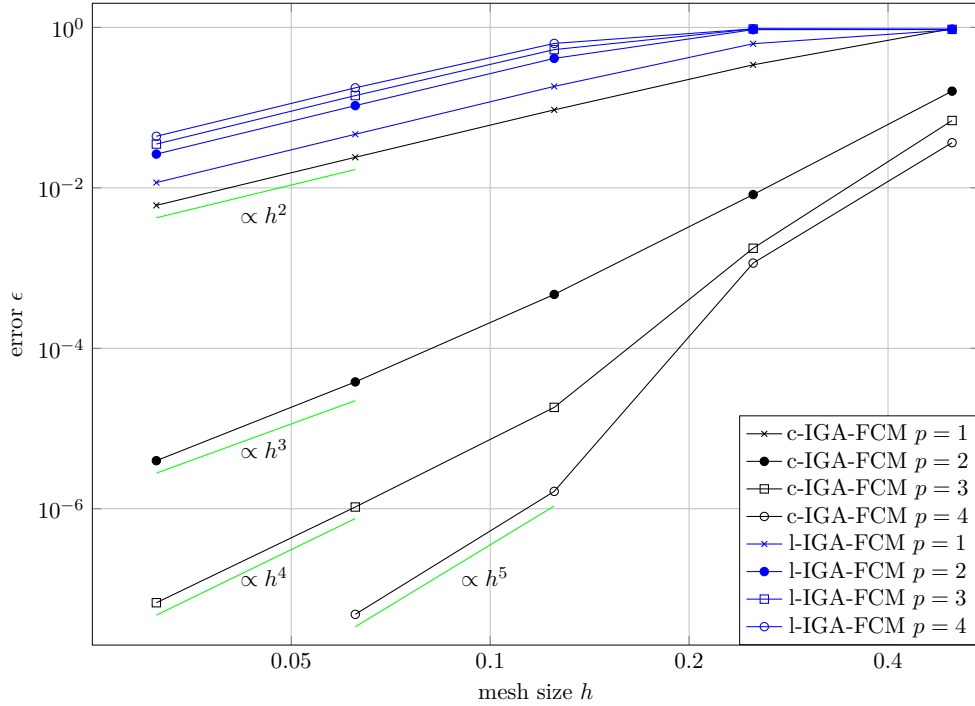


Figure 4: Convergence for consistent and lumped IGA-FCM with $p = 1, 2, 3, 4$

Corresponding to the results concerning the generalized eigenvalue problem in [50], a collapse of p -convergence can be observed for the problem at hand if the lumped version of IGA-FCM is applied. The order of convergence remains quadratic regardless of the polynomial order p , while the convergence constant even deteriorates as p increases. For the consistent version of IGA-FCM, however, we observe an increase in the order of convergence. As expected from results concerning the eigenfunction of the generalized eigenvalue problem, the error in time has an asymptotic convergence of $\mathcal{O}(h^{p+1})$ as well. Additionally, improvement in the constant can be noticed as p increases. Since FWI requires to temporarily store full wave fields, a memory-efficient solver is of great advantage. Thus, lumped IGA-FCM is not suitable for this application – and we will not consider it for the inverse problem, due to the higher number of degrees of freedom that is required to achieve a desired accuracy. However, consistent IGA-FCM provides a very memory-efficient and accurate solution of the wave problem and, therefore, is our method of choice from here on.

4 The inverse problem

4.1 Multi-resolution approach

To evaluate the applicability of the multi-resolution approach, we consider the embedded domain example of Figure 1. As given in [1], the sample has a size of $100\text{ mm} \times 50\text{ mm}$, density and wave speed are 2700 kg/m^3 and 6000 m s^{-1} , the lower boundary of the physical domain is defined by cubic splines interpolating the nine points $(0, 10\text{ mm})$, $(10\text{ mm}, 1\text{ mm})$, $(25\text{ mm}, 7.5\text{ mm})$, $(35\text{ mm}, 2\text{ mm})$, $(50\text{ mm}, 15\text{ mm})$, $(60\text{ mm}, 3\text{ mm})$, $(75\text{ mm}, 12\text{ mm})$, $(90\text{ mm}, 1\text{ mm})$, and $(100\text{ mm}, 10\text{ mm})$, the circular hole is centered at $(35\text{ mm}, 20\text{ mm})$ with radius $r = 7.5\text{ mm}$, and the unknown ellipse is located at $(63\text{ mm}, 18\text{ mm})$ with semi-axes $a = 6\text{ mm}$ and $b = 1\text{ mm}$, rotated by 67.5° . The sample is excited by 17 sources centered at the top surface with a spacing of 4 mm . Whenever a signal is sent from one of the sources, all source locations are used as receiver positions, mimicking the functionality of physical transducers. The central frequency of the 2-cycle sine burst is $f = 500\text{ kHz}$, corresponding to a dominant wavelength $\lambda_{\text{dom}} = 12\text{ mm}$. The synthetic reference data are computed with a boundary-conforming mesh of linear quadrilateral elements with over $50 \frac{\text{dof}}{\lambda_{\text{dom}}}$. The inversion is done using full matrix capture (FMC, see [56]) including signals of all sources, and a maximum of 10 iterations is performed. No regularization of the inverse problem beyond the intrinsic one associated to the discretization with B-splines is applied.

Taking into account the results of Section 3, the polynomial degree of the wave field is chosen to be $p = 2$ and $p = 3$. Wave field and material grids are discretized independently. The knot span length of the wave field mesh is varied between $h = 5\text{ mm}$, 2.5 mm , and 1.25 mm , leading to discretizations with 2.4, 4.8, and 9.6 knot spans per wavelength. These meshes are combined with independent grids of voxel size with $h^v = 1.25\text{ mm}$, 0.625 mm , or 0.3125 mm . The nine resulting combinations of the wave field and material grids are listed in Table 1. The number of voxels in each dimension per knot span is denoted as n^v . In order to incorporate the a priori known geometry the integration of the system matrices is carried out using a quadtree of depth $d = p + 1$ on each cut knot span. Inside the void domain, α is set to 10^{-5} and the inversion of γ is bounded between $\gamma_{\min} = 10^{-5}$ and $\gamma_{\max} = 1$. The wave field is computed for a time span of $6.0 \times 10^{-5}\text{ s}$ in 3000 time steps.

Table 1: Wave field and material grid sizes

	$h^v = 1.25\text{ mm}$	$h^v = 0.625\text{ mm}$	$h^v = 0.3125\text{ mm}$
$h = 5\text{ mm}$	$n^v = 4$	$n^v = 8$	$n^v = 16$
$h = 2.5\text{ mm}$	$n^v = 2$	$n^v = 4$	$n^v = 8$
$h = 1.25\text{ mm}$	$n^v = 1$	$n^v = 2$	$n^v = 4$

Figure 5 shows the inversion results for $p = 2$, Figure 6 for $p = 3$, and Table 2 and Table 3 list the computation times. For the graphical representation, the material field is visualized throughout the computational domain on the level of the applied voxel size. As noted above, the a priori known geometric features (i.e., the lower boundary and the circular hole) are resolved more precisely in the FCM computation by a quadtree integration.

If the wave field discretization is too coarse, dispersion errors cause imprecise wave simulations and consequently large artifacts in the material reconstruction. Regardless of the material resolution, the defect cannot be identified with a knot span size of $h = 5\text{ mm}$ and $p = 2$, see Figures 5a to 5c. The same holds for $p = 3$, see Figures 6a to 6c. Increasing the total number of knot spans improves the quality of the wave simulations and, consequently, mitigates the artifacts occurring in the inversions. While $h = 2.5\text{ mm}$ and $p = 2$ (Figures 5d to 5f) still lead to clearly visible artifacts, in particular to the right of the defect, $p = 3$ leads to a defect that is well distinguishable from the background (Figures 6d to 6f). For the finest meshes, the background perturbations almost completely disappear, see Figures 5g to 5i for $p = 2$ and Figures 6g to 6i for $p = 3$. The quality of the reconstructions in this case depends mainly on the resolution of the material field. Increasing the number of voxels

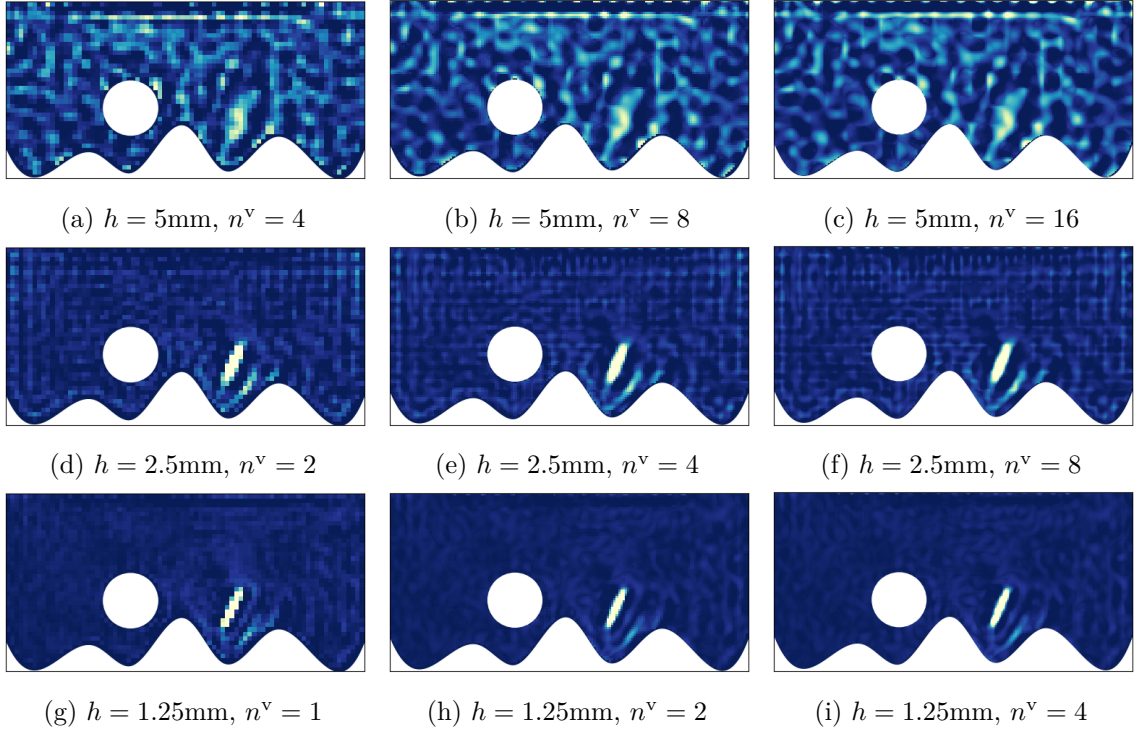


Figure 5: Inversion results for polynomial degree $p = 2$

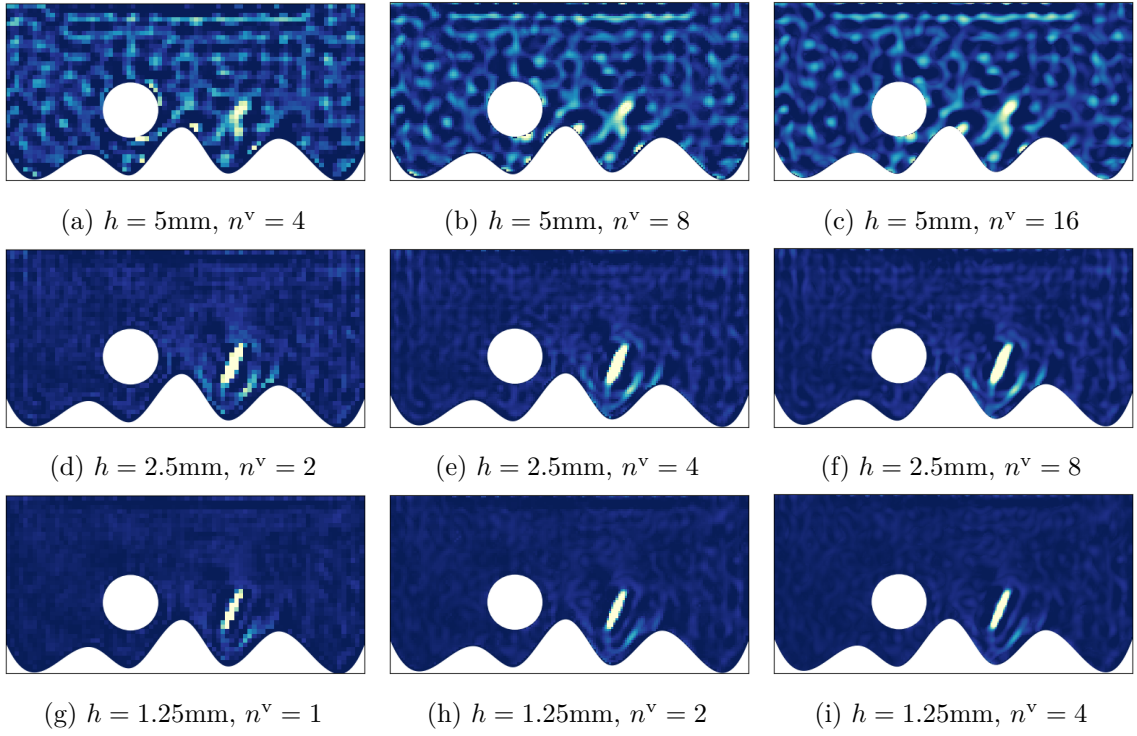


Figure 6: Inversion results for polynomial degree $p = 3$

Table 2: Computation times for polynomial degree $p = 2$

	$v = 1.25\text{mm}$	$v = 0.625\text{mm}$	$v = 0.3125\text{mm}$
$h = 5\text{mm}$	158.4 s	460.7 s	1648.5 s
$h = 2.5\text{mm}$	283.4 s	590.7 s	2219.9 s
$h = 1.25\text{mm}$	620.2 s	1007.7 s	2556.7 s

Table 3: Computation times for polynomial degree $p = 3$

	$v = 1.25\text{mm}$	$v = 0.625\text{mm}$	$v = 0.3125\text{mm}$
$h = 5\text{mm}$	268.4 s	790.5 s	2600.6 s
$h = 2.5\text{mm}$	425.1 s	965.4 s	3016.8 s
$h = 1.25\text{mm}$	990.8 s	1474.8 s	4004.5 s

leads to a better reconstruction of the defect boundary. This, however, comes at the cost of a much higher computational effort, note Table 2 for polynomial degree $p = 2$ and Table 3 for $p = 3$, since the sensitivity kernel (14) has to be evaluated at every voxel of the material grid. For example, considering column 1 (voxel size 1.25mm) of Table 2, the computational time is dominated by solving the wave fields. In contrast, column 3 (voxel size 0.3125mm) uses the same approximation of the wave fields, but now spends most of the optimization effort evaluating the gradient. The time measurements clearly confirm the complexity estimation of equation (17). Moreover, it can be seen that the reconstruction at undamaged regions is resolved quite well by a coarse voxel grid, since the reconstructed material does not vary largely. According to these observations, we suggest to use a locally refined material grid. The undamaged background can be resolved with a low number of voxels, while the areas of interest, i.e., where defects need to be detected, require a finer resolution. A corresponding refinement strategy and a suitable refinement indicator are presented in the following section.

4.2 Adaptive refinement of the material grid

For the refinement of the material grid, we introduce an indicator η corresponding to each voxel with value $\hat{\gamma}_i$. Motivated by Sobel filters, which are used in image processing [57], the L_2 -norm of the spatial gradient is used in [58] for the sharpness quantification of a reconstructed material parameter, i.e.,

$$\|\gamma(\mathbf{x})\|_2 = \sqrt{\left(\frac{\partial\gamma(\mathbf{x})}{\partial x}\right)^2 + \left(\frac{\partial\gamma(\mathbf{x})}{\partial y}\right)^2} \quad (22)$$

in two spatial dimensions.

High values indicate areas of rapidly changing material and, thus, boundaries of our regions of interest. Since the material parameter is discretized by constant shape functions defined on the voxel grid, we adapt the definition of the sharpness (22) to introduce a suitable indicator, replacing the derivatives in the spatial directions by $G_x(\hat{\gamma}_i)$ and $G_y(\hat{\gamma}_i)$. This voxelized gradient is computed as the mean of the absolute jump values of the material parameter γ between neighboring voxels, i.e.,

$$G_x(\hat{\gamma}_i) = \frac{1}{2h^v} \left(|\llbracket \hat{\gamma}_i \rrbracket^{(x,+)}| + |\llbracket \hat{\gamma}_i \rrbracket^{(x,-)}| \right) = \frac{1}{2h^v} (|\hat{\gamma}_r - \hat{\gamma}_i| + |\hat{\gamma}_i - \hat{\gamma}_l|) \quad (23)$$

$$G_y(\hat{\gamma}_i) = \frac{1}{2h^v} \left(|\llbracket \hat{\gamma}_i \rrbracket^{(y,+)}| + |\llbracket \hat{\gamma}_i \rrbracket^{(y,-)}| \right) = \frac{1}{2h^v} (|\hat{\gamma}_o - \hat{\gamma}_i| + |\hat{\gamma}_i - \hat{\gamma}_u|) \quad (24)$$

where h^v is the size of the voxel, $\hat{\gamma}_r$ is the voxel value of the voxel adjacent in positive x -direction and $\llbracket \hat{\gamma}_i \rrbracket^{(x,+)}$ is the jump of the material in that direction, $\hat{\gamma}_l$ and $\llbracket \hat{\gamma}_i \rrbracket^{(x,-)}$ are the voxel value and jump

in negative x -direction. Equivalently, $\hat{\gamma}_o$, $\hat{\gamma}_u$, $[\![\hat{\gamma}_i]\!](y,+)$ and $[\![\hat{\gamma}_i]\!](y,-)$ are used in y -direction. Finally, the indicator η of the voxel i with value $\hat{\gamma}_i$ is evaluated as

$$\eta(\hat{\gamma}_i) = \sqrt{(G_x(\hat{\gamma}_i))^2 + (G_y(\hat{\gamma}_i))^2}. \quad (25)$$

Using this indicator, we introduce an inversion framework with refinement. The basic ideas are shown in Figure 7. It can readily be extended to 3D-problems.

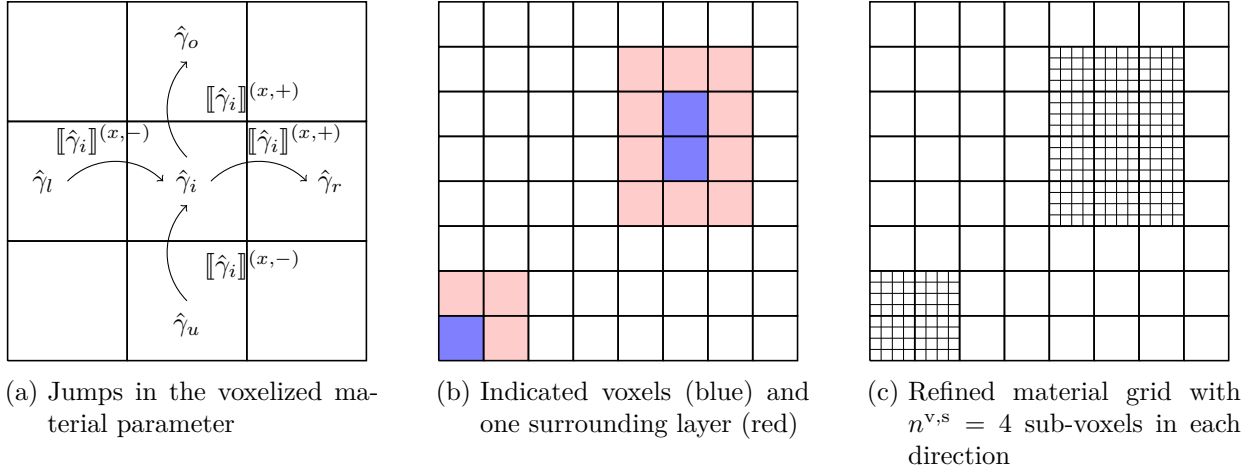


Figure 7: Refinement of the material grid

The reconstruction of the material parameter starts with an inversion on a coarse material grid with n^v voxels per knot span in each spatial direction. After $N^{i,1}$ iterations, the indicator is evaluated for each voxel of this intermediate solution and then compared to a threshold value τ . In the following examples, this threshold is set to half of the maximum occurring indicator value

$$\tau = \frac{1}{2} \arg \max_i \eta(\hat{\gamma}_i). \quad (26)$$

Since the material interfaces may not be perfectly identified yet, the indicated voxels and n^l surrounding layers are refined into $n^{v,s}$ sub-voxels per spatial direction. The parameter coefficients of the constant shape functions corresponding to these sub-voxels are included in the set of optimization variables. Finally, $N^{i,2}$ iterations are performed in a second inversion.

As in the previous section the example of Figure 1 is considered. Locally refined inversions are performed for a wave field discretization of $h = 1.25\text{mm}$ and polynomial degree $p = 2$ or $p = 3$. For the first $N^{i,1} = 3$ iterations, only one voxel per knot span is used to model the material, i.e., $n^v = 1$. This intermediate solution identifies the area of interest to be locally refined. The indicated voxels and one additional surrounding layer are subdivided into $n^{v,s} = 4$ sub-voxels in each spatial direction. From here, two different variants are investigated. In the first one, the intermediate solution of the first three iterations is chosen as the initial guess for the following $N^{i,2} = 7$ iterations. In the second variant, a full restart, the inversion is again performed for $N^{i,2} = 10$ iterations starting from homogeneous material. Figure 8 shows the results of the inversion with the introduced local refinement strategies for $p = 2$ and Figure 9 for $p = 3$. The intermediate results from the first three iterations, the corresponding sharpness and refined areas, and the final inversion results for both strategies are depicted. It is obvious that the reconstruction quality of the restart variant is superior to that of the start with an initial guess. The reason for this is that the intermediate reconstruction can be already trapped in a local minimum of the optimization process, which can yet not be refined to a minimum on the finer grid.

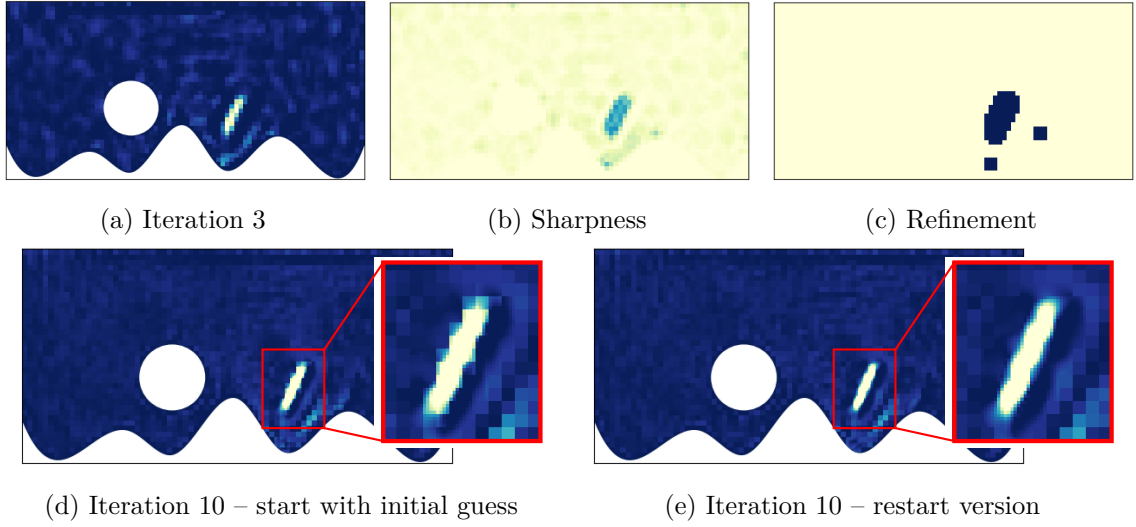


Figure 8: Inversion results with refinement – $h = 1.25\text{mm}$ and $p = 2$

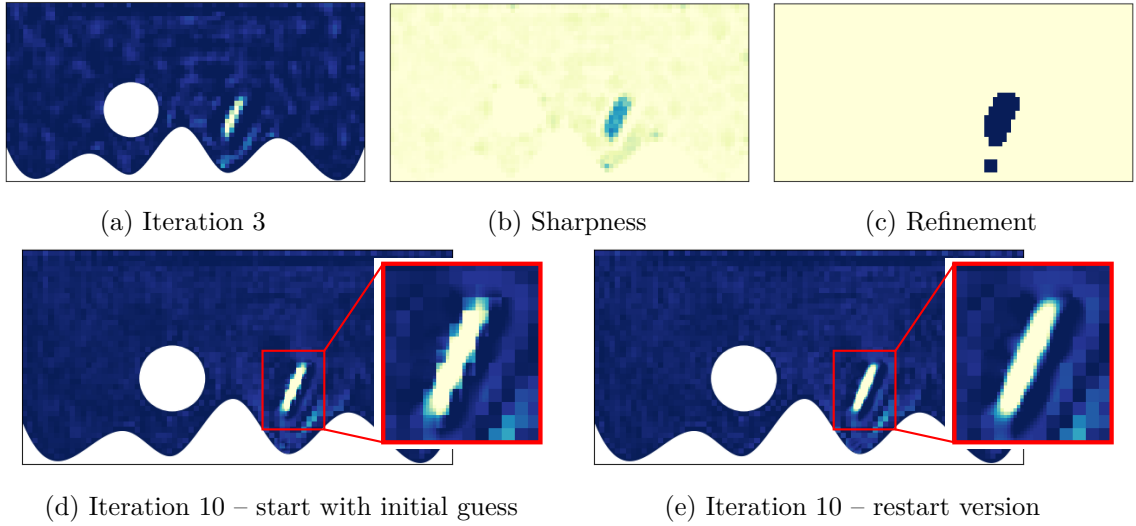


Figure 9: Inversion results with refinement – $h = 1.25\text{mm}$ and $p = 3$

Table 4 shows the computational times of the investigated refinement strategies. While the effort for the restart version is moderately larger than that of the refinement using the initial guess of the coarse material grid, both locally refined variants are over two times faster than the unrefined inversion. This is due to the fact that the computational effort for the gradient computation is greatly reduced. It should be noted that the restart version, in particular, does not compromise the quality of the reconstruction.

Table 4: Computation times with refinement for $h = 1.25\text{mm}$

	$p = 2$	$p = 3$
no refinement	2556.7 s	4004.5 s
refinement – start with initial guess	945.8 s	1328.8 s
refinement – restart version	1019.1 s	1813.5 s

4.3 3D example

The 3D structure under consideration is shown in Figure 10. The left pillar with the corresponding part of the roof (marked in blue) of the structure is examined locally in two inversions. The surface is given in STL (‘Standard Triangle Language’) format. At first only the left pillar is embedded in an extended computational domain of size $2\text{ m} \times 1.25\text{ m} \times 1.25\text{ m}$. The density is set to 2400 kg/m^3 , the wave speed to 3000 m s^{-1} . The setup of the inversion is shown in Figure 11.

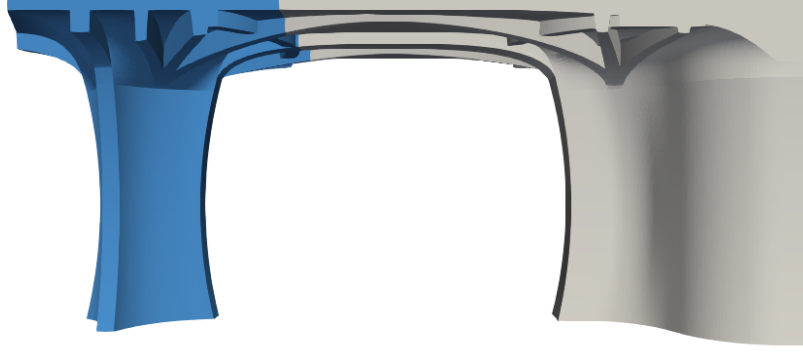


Figure 10: Investigated 3D structure [59]

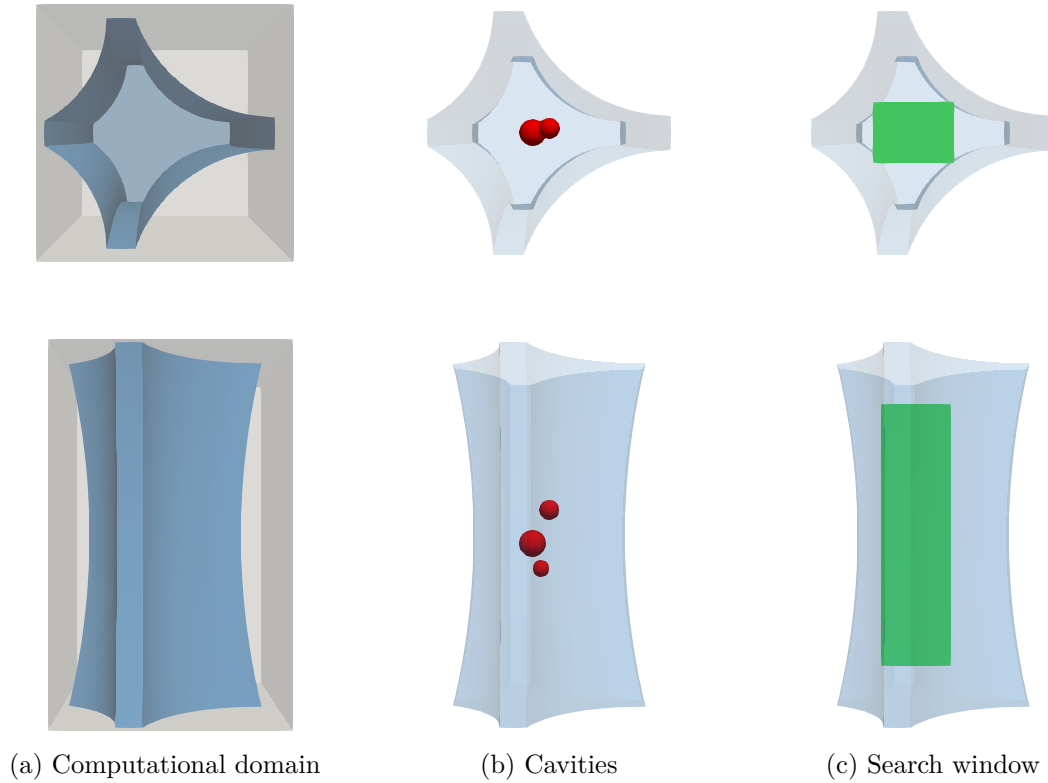


Figure 11: FWI setup of the left pillar: The structure is colored in blue, the computational domain in gray, the circular cavities in red, and the search window in green. Top views are given in the top pictures, while front views are displayed in the bottom pictures.

Three cavities are introduced at heights 0.8 m, 0.95 m, and 1.15 m with radii 0.05 m, 0.08 m, and 0.06 m. Reference data are generated for twelve sources placed in three different heights, i.e., 0.5 m, 1.0 m, and 1.5 m, using a mesh of quadratic B-splines with knot span size $h = 0.025\text{ m}$. Within the

void regions, α is set to 10^{-6} . Integration of the system matrices is performed with an octree of depth 3. The source term is a 2-cycle sine burst with a central frequency $f = 10$ kHz, resulting in a dominant wave length $\lambda_{\text{dom}} = 0.3$ m. In the inversion, the wave fields are discretized by cubic B-splines defined on a mesh with knot span size $h = 0.05$ m. The simulation of a time span of 8.0×10^{-4} s is carried out in 800 time integration steps. The material field is first defined on a grid with $n^v = 2$ voxels per knot span in each direction, before it is locally refined after $N^{i,1} = 3$ iterations with $n^{v,s} = 4$ sub-voxels per voxel in each direction. Integration of the system matrices is carried out on the voxel-level, incorporating the a priori known geometry by an octree of depth 4 for the cut knot spans with $\alpha = 10^{-5}$. Both local refinement strategies are executed – with either $N^{i,2} = 7$ additional iterations, if the intermediate solution is chosen as initial model for the subsequent optimization, or $N^{i,2} = 10$, if a homogeneous material is chosen as the new initial model. FWI can be applied to a region of interest by introducing a search window, see e.g., [14]. Consequently, γ is just optimized within the selected region. In this example, the search window has a size of $0.4 \text{ m} \times 0.3 \text{ m} \times 1.5 \text{ m}$ and is centered at 1 m height, mimicking the inner of the pillar. The optimization is bounded between $\gamma_{\text{min}} = 10^{-5}$ and $\gamma_{\text{max}} = 1$. The reconstructed cavities are shown in Figure 12. For a better visualization, the Iso Volume filter of ParaView was applied to the voxelized representation of the defects. The threshold in γ is set to 0.5 to classify void regions. Both strategies are suitable to precisely identify the positions and sizes of the defects. Also, the spherical shape of the voids is accurately approximated. In the restart version, the surface is reconstructed smoother due to the fact that the inversion is not trapped in a local minimum caused by the coarse material grid.

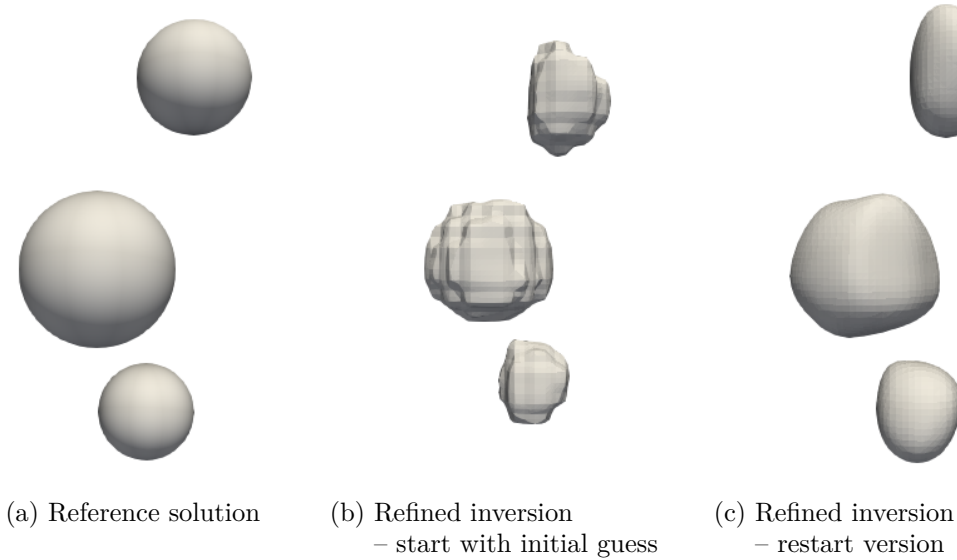


Figure 12: Reconstructed cavities in the left pillar

In a second inversion, the geometrically more complex left roof part is investigated. The FWI setup is shown in Figure 13. The physical domain is embedded in a computational domain of size $2.5 \text{ m} \times 2.5 \text{ m} \times 0.85 \text{ m}$. Nine sources are positioned on the top surface, while six sources are located on the bottom surface. To improve the inversion process, a search window is defined, excluding the areas where the sources are attached. In the reference model, an ellipsoidal cavity is placed at position $(1.35 \text{ m}, 1.2 \text{ m}, 0.6 \text{ m})$ with semi-axes 0.15 m , 0.075 m , and 0.075 m . The material parameters, spatial and time discretizations, and the source term remain the same as for the previous pillar example. Both refinement strategies are performed in the same manner as in the previous example. Figure 14 shows the identified cavities. In both strategies, the ellipsoid is detected at the right position with a proper shape. It has to be noted that the strategy that continues with the intermediate solution terminates after three refined iterations. The optimization is trapped in a local minimum and is not able to find a suitable update. Consequently, the size of the defect is slightly underestimated. On the other hand, the restart version successfully reproduces position, shape, and size of the cavity.

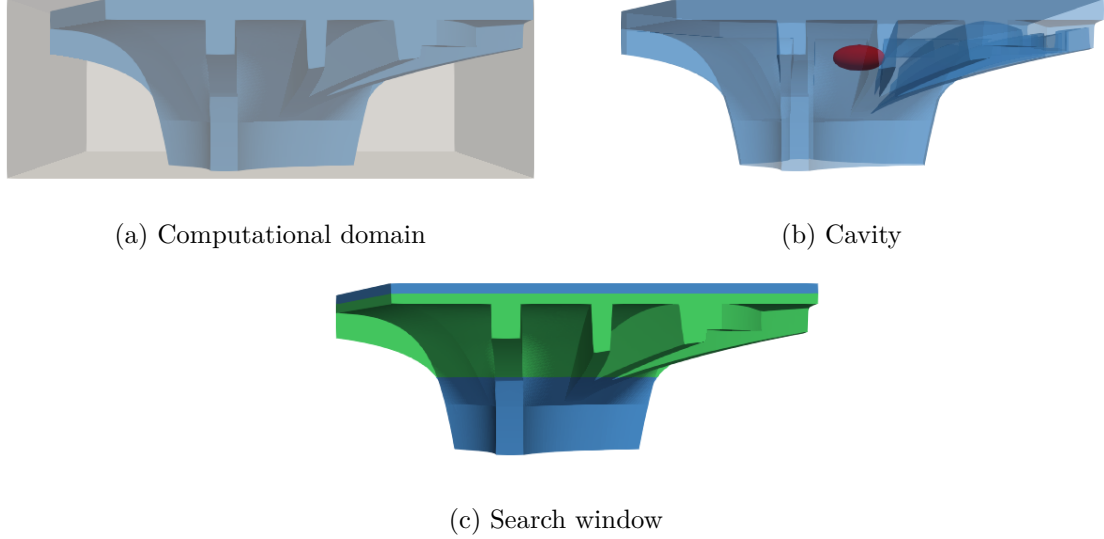


Figure 13: FWI setup of the left roof part: The structure is colored in blue, the computational domain in gray, the circular cavities in red, and the search window in green. Top views are given in the top pictures, while front views are displayed in the bottom pictures.

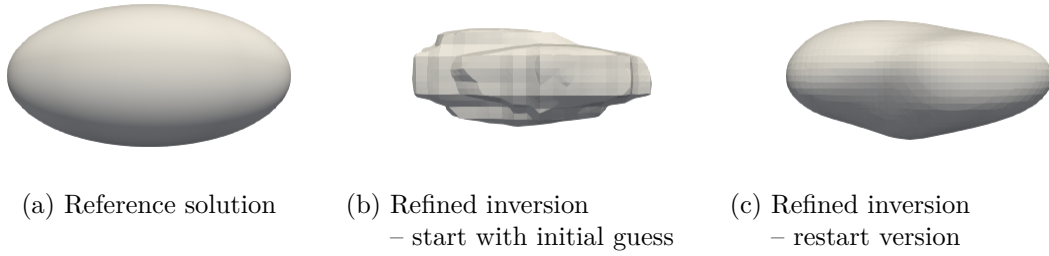


Figure 14: Reconstructed cavities in the roof

5 Conclusion

In the paper at hand, we propose a multi-resolution FWI approach based on a IGA-FCM discretization of the wave field and a voxelized representation of the material. In Section 3, an introductory investigation of the forward problem shows that IGA-FCM, used with a consistent mass matrix, is well-suited to solve the scalar wave equation precisely with a high accuracy per degree of freedom. Considering the inverse problem (Section 4), if the wave field is adequately resolved, the quality of the reconstruction mainly depends on the representation of the material field. By increasing the resolution of the independent material representation, a more precise identification of the defect boundaries is possible. However, this comes at the cost of rapidly increasing computation times, since the gradient has to be evaluated at each voxel. To mitigate this computational burden, we suggest a method to locally refine the material based on an indicator that accounts for the local changes of the material. The inversion is decomposed into a two-step optimization. At first, one optimization is performed on a coarse material grid. The resulting intermediate solution is then used to indicate regions of interest where the material field is refined. Finally, a second optimization is carried out on the locally refined material grid. The intermediate solution can serve as an initial model – or, alternatively, a restart is carried out starting with a homogeneous initial material. Particularly, the restart strategy leads to an accurate reconstruction of the defect’s location, size, and shape, despite coming at a slightly higher but still reasonable computational cost. Finally, the multi-resolution approach using local refinement is applied to a 3D specimen. Spherical and ellipsoidal cavities are identified and quantified accurately within a few iterations.

In summary, the paper at hand provides a framework that enables accurate and efficient FWI for the detection of void regions validated for synthetic reference data. IGA-FCM is used to discretize the wave field with a low number of degrees of freedom. The proposed indicator and refinement strategy of the material enables a precise and effective reconstruction of the defects. Our future research will further explore the potential and limits of this approach, in particular when it is applied to experimental data sets. Therefore, we plan to extend the framework to the elastic wave equation.

Acknowledgements

We gratefully thank the Deutsche Forschungsgemeinschaft (DFG, German Research Foundation) for their support through the grants KO 4570/1-1 and RA 624/29-1. We also thank Harald Kloft and Robin Dörrie from the Institut für Tragwerksentwurf of the Technische Universität Braunschweig for providing the geometric model investigated in Section 4.3 which serves as a benchmark in the DFG project 414265976 TRR 277.

References

- [1] T. Burchner, P. Kopp, S. Kollmannsberger, and E. Rank, “Immersed boundary parametrizations for full waveform inversion,” *Computer Methods in Applied Mechanics and Engineering*, vol. 406, p. 115893, 2023.
- [2] P. Lailly, “The seismic inverse problem as a sequence of before stack migrations,” *Conference on Inverse Scattering—Theory and Application, SIAM*, pp. 206–220, 1983.
- [3] A. Tarantola, “Inversion of seismic reflection data in the acoustic approximation,” *GEOPHYSICS*, vol. 49, no. 8, pp. 1259–1266, 1984.
- [4] D. Givoli, “A tutorial on the adjoint method for inverse problems,” *Computer Methods in Applied Mechanics and Engineering*, vol. 380, p. 113810, 2021.
- [5] A. Fichtner, *Full Seismic Waveform Modelling and Inversion*. Advances in Geophysical and Environmental Mechanics and Mathematics, Springer Berlin Heidelberg, 2011.
- [6] J. Virieux and S. Operto, “An overview of full-waveform inversion in exploration geophysics,” *GEOPHYSICS*, vol. 74, no. 6, pp. WCC1–WCC26, 2009.
- [7] D. Vigh and E. W. Starr, *Comparisons for waveform inversion, time domain or frequency domain?*, pp. 1890–1894. 2008.
- [8] R. G. Pratt, L. Huang, N. Duric, and P. J. Littrup, “Sound-speed and attenuation imaging of breast tissue using waveform tomography of transmission ultrasound data,” in *SPIE Medical Imaging*, 2007.
- [9] G. Y. S. Sandhu, E. West, C. Li, O. Roy, and N. Duric, “3d frequency-domain ultrasound waveform tomography breast imaging,” in *Medical Imaging*, 2017.
- [10] L. Guasch, O. Calderon Agudo, M.-X. Tang, P. Nachev, and M. Warner, “Full-waveform inversion imaging of the human brain,” *npj Digital Medicine*, vol. 3, 12 2020.
- [11] R. Seidl, *Full Waveform Inversion for Ultrasonic Nondestructive Testing*. PhD thesis, Technical University Munich, 2018.
- [12] J. Rao, M. Ratssepp, and Z. Fan, “Investigation of the reconstruction accuracy of guided wave tomography using full waveform inversion,” *Journal of Sound and Vibration*, vol. 400, pp. 317–328, 2017.
- [13] M. Lin, C. Wilkins, J. Rao, Z. Fan, and Y. Liu, “Corrosion detection with ray-based and full-waveform guided wave tomography,” in *Nondestructive Characterization and Monitoring of Advanced Materials, Aerospace, Civil Infrastructure, and Transportation XIV* (T.-Y. Yu, ed.), vol. 11380, pp. 102 – 109, International Society for Optics and Photonics, SPIE, 2020.
- [14] D. Rabinovich, D. Givoli, and E. Turkel, “Single-field identification of inclusions and cavities in an elastic medium,” *under review in International Journal for Numerical Methods in Engineering*, 2023.
- [15] A. Fichtner, B. L. N. Kennett, H. Igel, and H.-P. Bunge, “Full seismic waveform tomography for upper-mantle structure in the Australasian region using adjoint methods,” *Geophysical Journal International*, vol. 179, pp. 1703–1725, 12 2009.
- [16] A. Fichtner, J. Trampert, P. Cupillard, E. Saygin, T. Taymaz, Y. Capdeville, and A. Villaseñor, “Multiscale full waveform inversion,” *Geophysical Journal International*, vol. 194, pp. 534–556, 04 2013.
- [17] M. O. Deville, P. F. Fischer, and E. H. Mund, *High-Order Methods for Incompressible Fluid Flow*. Cambridge Monographs on Applied and Computational Mathematics, Cambridge University Press, 2002.
- [18] E. M. Rønquist and A. T. Patera, “A legendre spectral element method for the stefan problem,” *International Journal for Numerical Methods in Engineering*, vol. 24, no. 12, pp. 2273–2299, 1987.
- [19] S. Duczek and H. Gravenkamp, “Mass lumping techniques in the spectral element method: On the equivalence of the row-sum, nodal quadrature, and diagonal scaling methods,” *Computer Methods in Applied Mechanics and Engineering*, vol. 353, pp. 516–569, 2019.
- [20] T. Hughes, J. Cottrell, and Y. Bazilevs, “Isogeometric analysis: Cad, finite elements, nurbs, exact geometry and mesh refinement,” *Computer Methods in Applied Mechanics and Engineering*, vol. 194, no. 39, pp. 4135–4195, 2005.
- [21] T. J. Hughes, J. A. Evans, and A. Reali, “Finite element and nurbs approximations of eigenvalue, boundary-value,

- and initial-value problems,” *Computer Methods in Applied Mechanics and Engineering*, vol. 272, pp. 290–320, 2014.
- [22] A. Düster, E. Rank, and B. Szabó, “The p-Version of the Finite Element and Finite Cell Methods,” in *Encyclopedia of Computational Mechanics Second Edition* (E. Stein, R. Borst, and T. Hughes, eds.), pp. 1–35, 2017.
 - [23] E. Rank, M. Ruess, S. Kollmannsberger, D. Schillinger, and A. Düster, “Geometric modeling, isogeometric analysis and the finite cell method,” *Computer Methods in Applied Mechanics and Engineering*, vol. 249–252, pp. 104–115, 2012. Higher Order Finite Element and Isogeometric Methods.
 - [24] D. Schillinger, L. Dedè, M. A. Scott, J. A. Evans, M. J. Borden, E. Rank, and T. J. Hughes, “An isogeometric design-through-analysis methodology based on adaptive hierarchical refinement of nurbs, immersed boundary methods, and t-spline cad surfaces,” *Computer Methods in Applied Mechanics and Engineering*, vol. 249–252, pp. 116–150, 2012. Higher Order Finite Element and Isogeometric Methods.
 - [25] L. Leidinger, M. Breitenberger, A. Bauer, S. Hartmann, R. Wüchner, K.-U. Bletzinger, F. Duddeck, and L. Song, “Explicit dynamic isogeometric b-rep analysis of penalty-coupled trimmed nurbs shells,” *Computer Methods in Applied Mechanics and Engineering*, vol. 351, pp. 891–927, 2019.
 - [26] M. Meßmer, T. Teschemacher, L. F. Leidinger, R. Wüchner, and K.-U. Bletzinger, “Efficient cad-integrated isogeometric analysis of trimmed solids,” *Computer Methods in Applied Mechanics and Engineering*, vol. 400, p. 115584, 2022.
 - [27] E. Burman, S. Claus, P. Hansbo, M. G. Larson, and A. Massing, “Cutfem: Discretizing geometry and partial differential equations,” *International Journal for Numerical Methods in Engineering*, vol. 104, no. 7, pp. 472–501, 2015.
 - [28] E. Burman, P. Hansbo, and M. G. Larson, “Explicit time stepping for the wave equation using cutfem with discrete extension,” *SIAM Journal on Scientific Computing*, vol. 44, no. 3, pp. A1254–A1289, 2022.
 - [29] S. Duczek, M. Jouliaian, A. Düster, and U. Gabbert, “Numerical analysis of lamb waves using the finite and spectral cell methods,” *International Journal for Numerical Methods in Engineering*, vol. 99, no. 1, pp. 26–53, 2014.
 - [30] M. Jouliaian, S. Duczek, U. Gabbert, and A. Düster, “Finite and spectral cell method for wave propagation in heterogeneous materials,” *Computational Mechanics*, vol. 54, 2014.
 - [31] L. Leidinger, *Explicit Isogeometric B-Rep Analysis for Nonlinear Dynamic Crash Simulations*. PhD thesis, Technical University Munich, 2020.
 - [32] S. K. Stoter, S. C. Divi, E. H. van Brummelen, M. G. Larson, F. de Prenter, and C. V. Verhoosel, “Critical time-step size analysis and mass scaling by ghost-penalty for immersogeometric explicit dynamics,” *Computer Methods in Applied Mechanics and Engineering*, vol. 412, p. 116074, 2023.
 - [33] S. Sticko, G. Ludvigsson, and G. Kreiss, “High-order cut finite elements for the elastic wave equation,” *Advances in Computational Mathematics*, vol. 46, 05 2020.
 - [34] M. Breitenberger, A. Apostolatos, B. Philipp, R. Wüchner, and K.-U. Bletzinger, “Analysis in computer aided design: Nonlinear isogeometric b-rep analysis of shell structures,” *Computer Methods in Applied Mechanics and Engineering*, vol. 284, pp. 401–457, 2015. Isogeometric Analysis Special Issue.
 - [35] S. Badia, F. Verdugo, and A. F. Martín, “The aggregated unfitted finite element method for elliptic problems,” *Computer Methods in Applied Mechanics and Engineering*, vol. 336, pp. 533–553, 2018.
 - [36] E. Nadal, J. J. Ródenas, J. Albelda, M. Tur, J. E. Tarancón, and F. J. Fuenmayor, “Efficient Finite Element Methodology Based on Cartesian Grids: Application to Structural Shape Optimization,” *Abstract and Applied Analysis*, vol. 2013, no. SI51, pp. 1 – 19, 2013.
 - [37] A. Main and G. Scovazzi, “The shifted boundary method for embedded domain computations. part i: Poisson and stokes problems,” *Journal of Computational Physics*, vol. 372, pp. 972–995, 2018.
 - [38] A. Main and G. Scovazzi, “The shifted boundary method for embedded domain computations. part ii: Linear advection–diffusion and incompressible navier–stokes equations,” *Journal of Computational Physics*, vol. 372, pp. 996–1026, 2018.
 - [39] A. Düster, J. Parvizian, Z. Yang, and E. Rank, “The finite cell method for three-dimensional problems of solid mechanics,” *Computer Methods in Applied Mechanics and Engineering*, vol. 197, no. 45, pp. 3768–3782, 2008.
 - [40] M. Pető, F. Duvigneau, and S. Eisenträger, “Enhanced numerical integration scheme based on image-compression techniques: application to fictitious domain methods,” *Advanced Modeling and Simulation in Engineering Sciences*, vol. 7, 2020.
 - [41] M. Jouliaian, S. Hubrich, and A. Düster, “Numerical integration of discontinuities on arbitrary domains based on moment fitting,” *Comput. Mech.*, vol. 57, p. 979–999, jun 2016.
 - [42] T.-P. Fries and S. Omerović, “Higher-order accurate integration of implicit geometries,” *International Journal for Numerical Methods in Engineering*, vol. 106, no. 5, pp. 323–371, 2016.
 - [43] L. Kudela, N. Zander, S. Kollmannsberger, and E. Rank, “Smart octrees: Accurately integrating discontinuous functions in 3d,” *Computer Methods in Applied Mechanics and Engineering*, vol. 306, 04 2016.
 - [44] Z. Yang, M. Ruess, S. Kollmannsberger, A. Düster, and E. Rank, “An efficient integration technique for the voxel-based finite cell method,” *International Journal for Numerical Methods in Engineering*, vol. 91, no. 5, pp. 457–471, 2012.
 - [45] N. Korshunova, G. Alaimo, S. Hosseini, M. Carraturo, A. Reali, J. Niiranen, F. Auricchio, E. Rank, and S. Kollmannsberger, “Image-based numerical characterization and experimental validation of tensile behavior of octet-truss lattice structures,” *Additive Manufacturing*, vol. 41, 03 2021.
 - [46] J. A. Cottrell, T. J. Hughes, and Y. Bazilevs, *Isogeometric analysis: toward integration of CAD and FEA*. John Wiley & Sons, 2009.
 - [47] C. de Boor, *A Practical Guide to Spline*, vol. Volume 27. Applied Mathematical Sciences, Springer, New York, 01 1978.

- [48] E. Cohen, R. Riesenfeld, and G. Elber, *Geometric Modeling with Splines: An Introduction*. USA: A. K. Peters, Ltd., 2001.
- [49] Y. Voet, E. Sande, and A. Buffa, “A mathematical theory for mass lumping and its generalization with applications to isogeometric analysis,” 2022.
- [50] J. A. Cottrell, A. Reali, Y. Bazilevs, and T. J. R. Hughes, “Isogeometric analysis of structural vibrations,” *Computer Methods in Applied Mechanics and Engineering*, vol. 195, no. 41, pp. 5257–5296, 2006.
- [51] T. J. Hughes, *The finite element method: linear static and dynamic finite element analysis*. Courier Corporation, 2012.
- [52] A. Fichtner, H.-P. Bunge, and H. Igel, “The adjoint method in seismology: I. theory,” *Physics of the Earth and Planetary Interiors*, vol. 157, no. 1, pp. 86–104, 2006.
- [53] A. Fichtner, H.-P. Bunge, and H. Igel, “The adjoint method in seismology—: II. applications: traveltimes and sensitivity functionals,” *Physics of the Earth and Planetary Interiors*, vol. 157, no. 1, pp. 105–123, 2006.
- [54] J. Nocedal and S. Wright, *Numerical Optimization*. Springer Series in Operations Research and Financial Engineering, Springer New York, 2006.
- [55] P. Virtanen, R. Gommers, T. E. Oliphant, M. Haberland, T. Reddy, D. Cournapeau, E. Burovski, P. Peterson, W. Weckesser, J. Bright, S. J. van der Walt, M. Brett, J. Wilson, K. J. Millman, N. Mayorov, A. R. J. Nelson, E. Jones, R. Kern, E. Larson, C. J. Carey, Í. Polat, Y. Feng, E. W. Moore, J. VanderPlas, D. Laxalde, J. Perktold, R. Cimrman, I. Henriksen, E. A. Quintero, C. R. Harris, A. M. Archibald, A. H. Ribeiro, F. Pedregosa, P. van Mulbregt, and SciPy 1.0 Contributors, “SciPy 1.0: Fundamental Algorithms for Scientific Computing in Python,” *Nature Methods*, vol. 17, pp. 261–272, 2020.
- [56] C. Clark, B. Drinkwater, and P. Wilcox, “The post-processing of ultrasonic array data using the total focusing method,” *Insight - Non-Destructive Testing and Condition Monitoring*, vol. 46, pp. 677–680, 11 2004.
- [57] R. Gonzalez and R. Woods, *Digital Image Processing Global Edition*. Pearson Deutschland, 2017.
- [58] L. Herrmann, T. Burchner, F. Dietrich, and S. Kollmannsberger, “On the use of neural networks for full waveform inversion,” 2023.
- [59] H. Kloft and R. Dörrie, “Shelltonic benchmark.” Additive Manufacturing in Construction, <https://amc-trr277.de>, 2023.